ISSN 1054-660X, Laser Physics, 2012, Vol. 22, No. 9, pp. 1439–1444.

Estimation of Shear Wave Velocity in Gelatin Phantoms Utilizing PhS-SSOCT[1]

Ravi Kiran Manapuram[a], S. Aglyamov[b], F. M. Menodiado[c], M. Mashiatulla[c], Shang Wang[c], S. A. Baranov[c], Jiasong Li[c], S. Emelianov[b], and K. V. Larin[a, c, d, *]

[a] *Department of Mechanical Engineering, University of Houston, N207 Engineering Building 1, Houston, TX 77204, USA*

[b] *Department of Biomedical Engineering, University of Texas at Austin, Austin, TX, 78712, USA*

[c] *Department of Biomedical Engineering, University of Houston, 3605 Cullen Blvd, SERC Bldg, Houston, TX77204, USA*

[d] *Institute of Optics and Biophotonics, Saratov State University, Saratov, 410012 Russia*

*e-mail: klarin@uh.edu

Received February 24, 2012; in final form, May 2, 2012; published online August 1, 2012

Abstract—We report a method for measuring shear wave velocity in soft materials using phase stabilized swept source optical coherence tomography (PhS-SSOCT). Wave velocity was measured in phantoms with various concentrations of gelatin and therefore different stiffness. Mechanical waves of small amplitudes (~10 μm) were induced by applying local mechanical excitation at the surface of the phantom. Using the phase-resolved method for displacement measurement described here, the wave velocity was measured at various spatially distributed points on the surface of the tissue-mimicking gelatin-based phantom. The measurements confirmed an anticipated increase in the shear wave velocity with an increase in the gelatin concentrations. Therefore, by combining the velocity measurements with previously reported measurements of the wave amplitude, viscoelastic mechanical properties of the tissue such as cornea and lens could potentially be measured.

DOI: 10.1134/S1054660X12090101

1. INTRODUCTION

Changes in mechanical properties of tissue may be indicative of natural aging processes as well as pathological changes associated with a disease. As a result, several approaches in elasticity imaging and sensing were developed and applied in various fields such as cardiovascular medicine, orthopedics, ophthalmology, restorative dentistry, developmental biology, tissue engineering, regenerative medicine cancer diagnosis and treatment [1–3]. For example in ophthalmology, elasticity imaging could potentially be used in evaluating the biomechanical properties of cornea pre- and post-surgical procedures, guiding corneal surgery as well as tracking the healing progress [4–6]. Early clinical diagnosis of corneal ectatic diseases and glaucoma can also be attained from measurements of mechanical properties of tissue [7–9].

Out of several techniques developed for elastography, optical elasticity imaging or elastography has developed into a well-established modality due to its capability of providing images with high spatial resolution. Various optical techniques such as speckle tracking [10], contrast imaging methods [11–13] and multi modal techniques (e.g., acousto-optical elastography [14]) have been applied in optical elastography. Fibered confocal fluorescence microscopy (FCFM) [15, 16] allows elastography at cellular level. However, due to limited imaging depth, optical elastography with the above mentioned techniques are limited only to superficial tissue layers.

Optical coherence tomography (OCT) is a non-invasive optical imaging modality that allows high speed and high resolution 3D imaging of tissue structures at a depth of ~2–3 mm. Since its introduction in 1991, OCT elastography has been first demonstrated by Schmitt in 1998 [17], where microscopic deformation due to compressive stress has been studied. Since then OCT has been further developed and applied to track tissue displacements by incorporating various optical techniques such as speckle tracking [18, 19], correlation [20–22], Doppler and phase methods [21–23]. However, application of compressive stress is not feasible to the eye, thus limiting their application in vivo. In an effort to obtain in vivo measurements in the eye, Alonso-Caneiro et al., have used air puff stimulation and recorded corneal dynamics using swept source optical coherence tomography [24]. However, relatively high displacement (~1 mm) was used to obtain accurate results. Recently, Li et al., have utilized laser ultrasound (LUS) to generate surface acoustic waves (SAW) and measured the wave param-

[1] The article is published in the original.

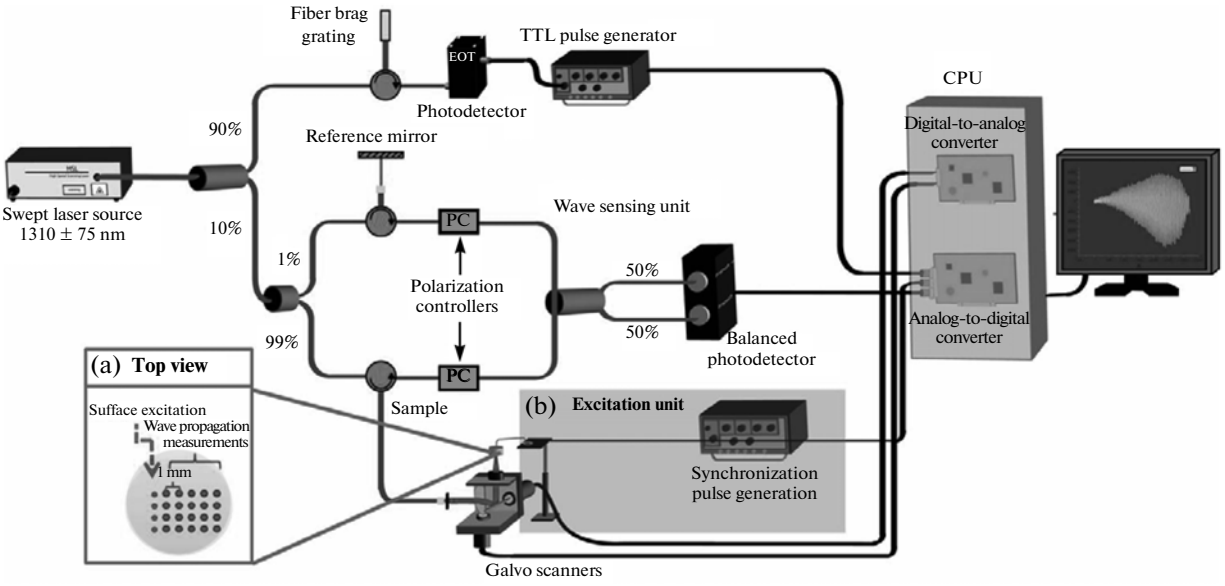

Fig. 1. Schematic of the experimental system based on phase-sensitive swept-source OCT. Insert (a) shows the top view of the phantom surface indicating the location of surface excitation (small dots) and wave propagation measurements (bold dots). Insert (b) shows the source of excitation.

eters using OCT [25]. Although they have achieved detection sensitivity around 10 nm (same as in our case) they used relatively high energy from the laser (~3 mJ) to excite the mechanical response of tissue—this level of energy may be too high for soft delicate tissues such as cornea. Nevertheless, OCT elastography has been already used clinically to detect coronary diseases and skin lesions [14, 18, 26]. In order to utilize OCT elastography in ophthalmology where relatively low amplitude of mechanical excitation is required, an approach capable of measurements with of high sensitivity is required. Previously, we have demonstrated the application of phase stabilized swept source optical coherence tomography (PhS-SSOCT) in measuring nanometer level amplitudes in murine eye lens [27, 28]. In this paper, we utilize the PhS-SSOCT to demonstrate the possibility of measuring propagation of mechanical waves in tissue-mimicking phantoms. Once developed, the same approach could be utilized for measuring nanometer amplitude mechanical waves in ocular tissues making it possible to assess the biomechanical properties of tissue non-invasively.

2. MATERIALS AND METHODS

2.1. The Experimental Set Up

The PhS-SSOCT elastography system is shown in Fig. 1. The mechanical waves were generated in the excitation unit by tapping the sample with a tip of a thin wire. The wire was attached to a speaker diaphragm that responds to a pulse generated using a pulse generator. Every time a pulse was generated, the wire vibrated and the tip of the wire touched the sample thus introducing mechanical waves. The pulse generator was preset to generate ~1 ms pulse every 2 s and the output of the generator was used both to vibrate the diaphragm and to record the beginning of the pulse. The wave propagation was measured using a phase stabilized swept source OCT system (PhS-SSOCT). The details of PhS-SSOCT are described elsewhere [28, 29]. Briefly, the PhS-SSOCT consisted of two Mach Zehnder interferometers (MZI); one for imaging and other for linear *k*-space calibration. For this study, the PhS-SSOCT was modified to enable synchronization between the wave induction and data acquisition. Synchronization was achieved by recording the excitation pulse simultaneously with data acquisition. The *k*-space calibration arm was replaced with the excitation unit to enable pulse recording and data acquisition simultaneously. The *k*-space calibration was performed with the pre-generated data as following: the sample was replaced with a mirror and the path difference between the sample mirror and the reference mirror was kept at an optimal distance that resulted in the highest resolution after calibration. Real fringes were converted to the complex domain using Hilbert transformation [30]. The unwrapped phase differences were extracted from these complex fringes. The coefficients utilized to linearize the unwrapped phases (calibration coefficients) were saved and used to convert the raw OCT data to linear *k*-space. Although this procedure does not allow dynamic calibration, the calibration coefficients were obtained before every experiment making the method quasi-dynamic. With this procedure, the system was capable of a depth resolution of ~8 μm, imaging depth of 4.5 mm, phase sta-

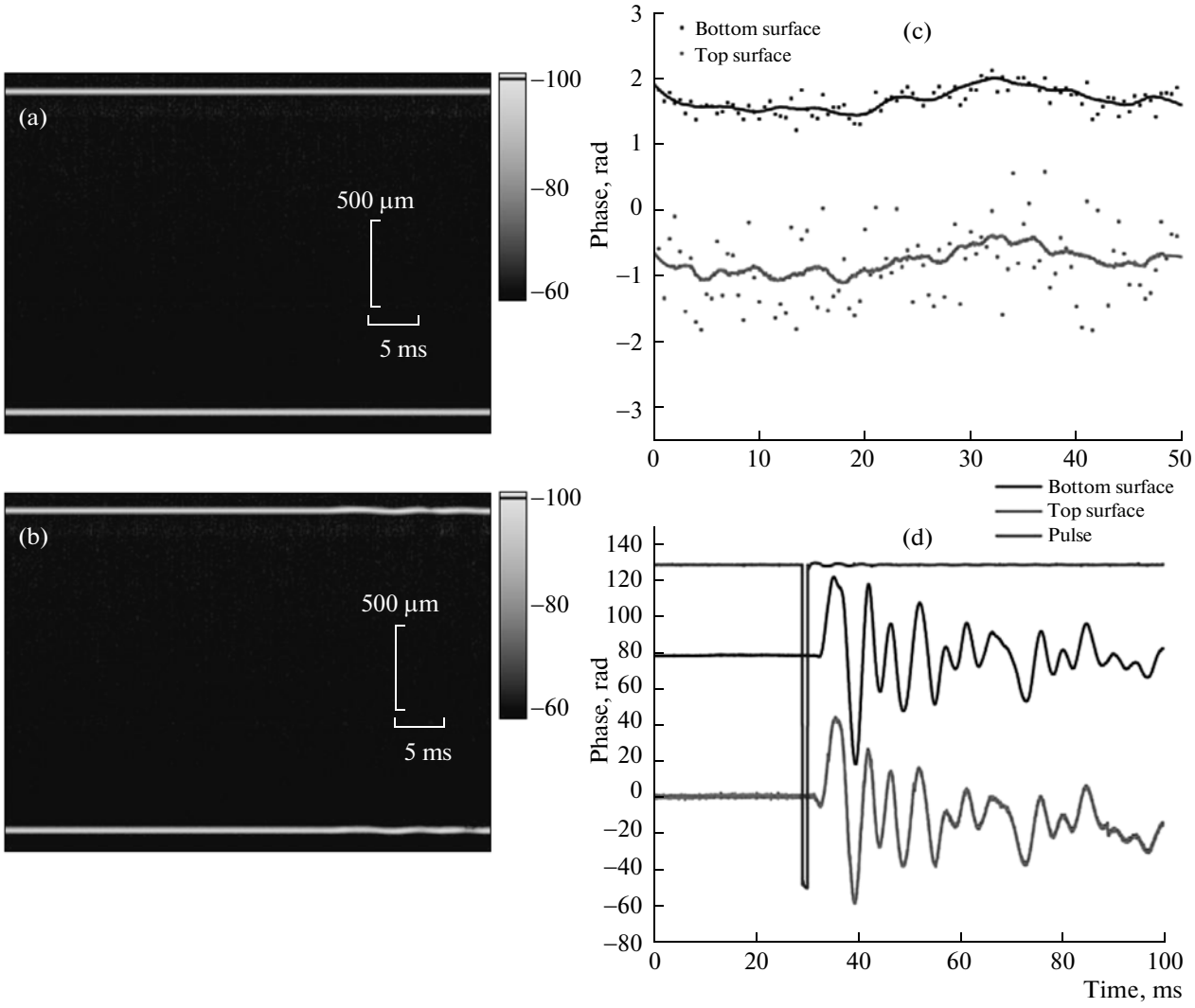

Fig. 2. M-mode images (a, b) and corresponding temporal measurements of phase of OCT signal (c, d) acquired at the surface of (a, c) stationary phantom (i.e., phantom was not subjected to any external mechanical excitation) and (b, d) phantom before, during and after the application of localized mechanical excitation at the surface.

bility of 0.04 rad (that translates to 9 nm of displacement sensitivity) and time resolution of 33 μs.

2.2. Preparation of Gelatin Phantoms

In order to simulate soft tissue samples of controlled stiffness, gelatin phantoms with varying concentrations (8–16% w/v) were prepared. Gelatin (P8 Gummi gelatin 250 Bloom, RB Leiner) was mixed with water at 60°C until all granules were dissolved. Care has to be taken while stirring the mixture to avoid bubbles from forming in order to avoid changes in wave propagation due to bubbles in the phantom. The mixture was poured into a mold to create ~1 mm thick layer, and cooled in the refrigerator for 30 min (~10°C) [31]. The solidified gel formed a solid slab that served as a tissue mimicking sample. It is known that the higher is the gelatin concentration, the greater is the stiffness of gel. We verified the elastic properties of the samples using the uniaxial stress-strain measurements performed using In-Spec 2200 (Instron, Inc., Norwood, MA).

2.3. Experimental Procedure and Detection of Mechanical Waves

Mechanical waves were introduced on the phantom surface using the wire-based mechanical excitation unit described earlier. The excitation points are shown in insert in Fig. 1 (small dots). Waves propagated in all directions creating internal and surface displacements in the phantom. The displacements were recorded at several points spaced 1 mm from each other shown in insert in the Fig. 1 (bold circles). Velocity was calculated by measuring the temporal characteristics of the induced mechanical waves.

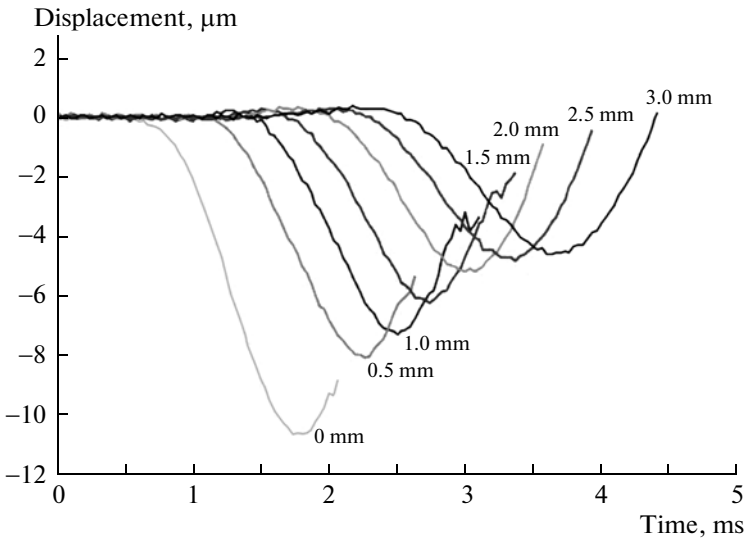

Fig. 3. Phase responses recorded at 0 to 3 mm distances away from the source of excitation in 8% gelatin phantom.

To perform these measurements, the PhS-SSOCT was operated in M-mode (OCT A-scans at fixed position over time) where each M-mode image was acquired for 50 ms. Figures 2a and 2b show the M-mode images of the phantom before, during, and after the mechanical excitation, correspondingly. Both surfaces of the phantom could be seen in M-mode images. From the M-mode image, phases were estimated from both surfaces of the phantom (details of phase measurements can be found elsewhere [27, 28]). The phases are nearly constants with insignificant variations when the sample is not excited as shown in Fig. 2c. However, when mechanical excitation is applied externally, phases at the boundaries change as shown in the Fig. 2d. Amplitude of induced displacements is low and hardly noticeable in M-mode image (Fig. 2b). The displacement amplitudes were quantified from the phase measurements using the relation shown in Eq. (1)

$$V = \frac{\lambda}{2\pi}\varphi, \qquad (1)$$

where φ is a phase (radians), λ is a wavelength (nm), and V is a displacement amplitude (nm).

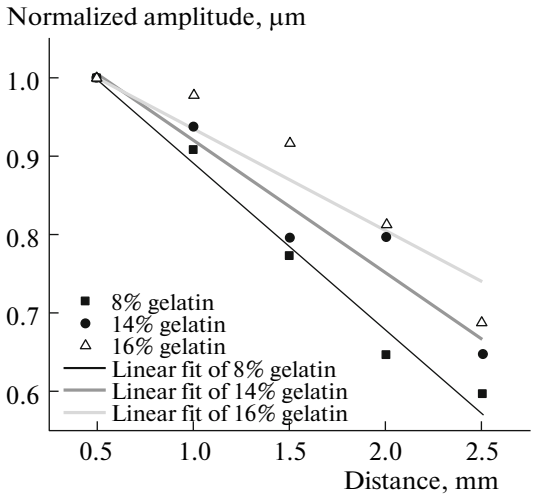

Fig. 4. Amplitudes of the wave recorded at increasing distances from the source of excitation.

3. QUANTIFYING METHOD

Shear wave velocities were quantified from the time delays calculated at the measuring points. To obtain the time delay, the pulse from a function generator used to excite the phantom was recorded using the second channel of ADC (Fig. 1). The delay between the generation of the excitation pulse and the wiretapping was recorded using the following procedure: the imaging objective in the sample arm was inverted such that the wire can be imaged directly through the phantom allowing direct monitoring of the wire from the image. The phase response at the point of tapping on the top surface of the phantom gives the exact time of excitation as shown in the Fig. 2d. The blue trace in the Fig. 2d shows the time of occurrence of the pulse to excite the phantom. The red and black traces are the phase responses at the top and bottom surfaces of the phantom at the point where the wire touches the phantom surface. The time delay between the occurrence of the pulse and the phase response gives the total time taken for the pulse to excite the speaker diaphragm and the wire. All the delay measurements were performed relative to the pulse.

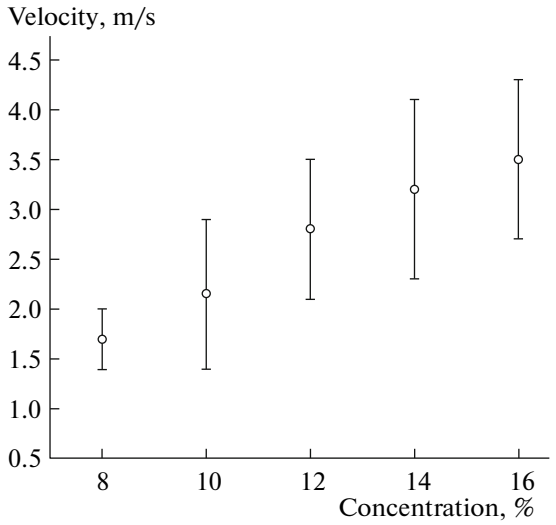

Fig. 5. Shear wave velocities measured at the surface of the 8–16% gelatin phantoms. The bars represent the standard deviation with $N = 3$.

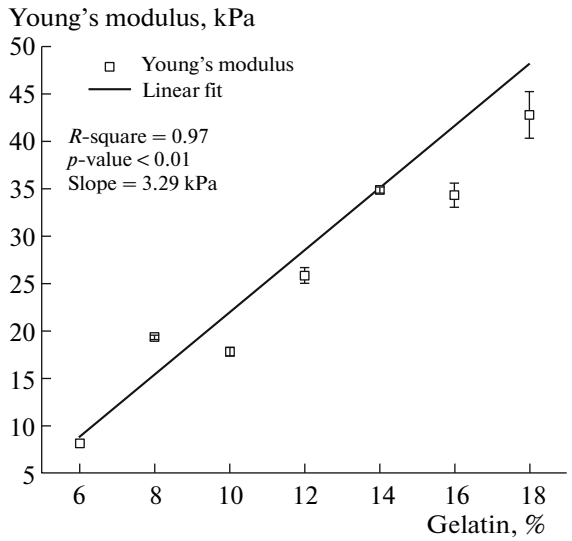

Fig. 6. Young's modulus vs. gelatin concentration obtained using uniaxial tests.

4. RESULTS AND DISCUSSION

Figure 3 depicts typical phase responses collected at increasing distances from the point of excitation in 8% phantom. First, these data clearly demonstrate attenuation of the wave amplitude as it propagates on the surface of the phantom away from the excitation point. Second, the time delay for the wave reaching different locations could be used to calculate wave velocity. For example, in Fig. 3, there is a time delay of ~0.28 ms between the phase responses recorded at 1.0 and 0.5 mm that gives the velocity of 1.7 m/s.

The attenuation of the wave amplitude with the increasing distance from the point of wave excitation for 8–16% gelatin concentrations is shown in Fig. 4. As expected, the wave amplitude decreases with the increasing distance from the point of tapping for all phantoms. The amplitude of the wire motion was not controlled in the experiments; therefore the initial amplitude at zero position was an arbitrary value. Combination of measurements of the wave's amplitude attenuation together with its velocity could be used to attain viscoelastic properties of the sample.

The velocity of the propagating shear waves in phantoms with varying concentration of gelatin is shown in Fig. 5. The values shown represent the velocities averaged over a 3 mm range. Clearly, as depicted in Fig. 5, shear wave velocity increases with the increase in gelatin concentration. These results were validated by direct stress-strain measurements using In-Spec 2200 portable system as shown in Fig. 6. Thus, the results presented in Figs. 5, 6 demonstrate that the PhS-SSOCT elasticity imaging method is capable of quantifying shear wave velocity and, therefore, shear or Young's modulus of the tissue.

The accuracy of the described method for quantification of amplitude and speed of the mechanical wave depends on phase-stability of the system and signal acquisition speed, respectively. The results in this paper clearly demonstrate possibility of quantification of low-amplitude (micrometer-scale) mechanical waves with possibility to go down to nanometer scale. However, the signal acquisition speed of the described SSOCT system is 30 kHz which limits detection of high frequency waves generated on the surfaces of the cornea. Therefore, incorporating higher speed swept laser sources would increase accuracy of the wave characterization.

5. CONCLUSIONS

In this paper we demonstrated possibility for non-invasive quantification of both amplitude and velocity of propagating mechanical waves in gelatin materials. Phase-sensitive analysis of the amplitudes allowed quantification of micrometer-scale perturbations, therefore showing promise of this method being applied to soft delicate biological tissues such as cornea, sclera, and crystalline lens of the eye. Our future studies will be focused on translating this method to biological tissues and development analytical model that can provide viscoelastic properties of the object based on the attenuation and velocity of the shear waves.

REFERENCES

1. K. J. Parker, M. M. Doyley, and D. J. Rubens, "Imaging the Elastic Properties of Tissue: the 20 Year Perspective," Phys. Med. Biol. **56** (1), R1–R29 (2011).

2. J. F. Greenleaf, M. Fatemi, and M. Insana, "Selected Methods for Imaging Elastic Properties of Biological Tissues," Annu. Rev. Biomed. Eng. **5**, 57–78 (2003).
3. A. Sarvazyan, T. J. Hall, M. W. Urban, et al., "An Overview of Elastography-An Emerging Branch of Medical Imaging," Curr. Med. Imaging Rev. **7** (4), 255–282 (2011).
4. K. W. Hollman, S. Y. Emelianov, J. H. Neiss, et al., "Strain Imaging of Corneal Tissue with an Ultrasound Elasticity Microscope," Cornea **21** (1), 68–73 (2002).
5. T. Juhasz, F. H. Loesel, R. M. Kurtz, et al., "Corneal Refractive Surgery with Femtosecond Lasers," IEEE J. Selected Topics Quant. Electron. **5** (4), 902–910 (1999).
6. M. Tanter, D. Touboul, J. L. Gennisson, et al., "High-Resolution Quantitative Imaging of Cornea Elasticity Using Supersonic Shear Imaging," Med. Imaging, IEEE Trans. **28** (12), 1881–1893 (2009).
7. I. F. Comaish and M. A. Lawless, "Progressive Post-LASIK Keratectasia: Biomechanical Instability or Chronic Disease Process?," J. Cataract. Refract. Surg. **28** (12), 2206–2213 (2002).
8. W. J. Dupps, Jr., "Biomechanical Modeling of Corneal Ectasia," J. Refract. Surg. **21** (2), 186–190 (2005).
9. J. Liu and C. J. Roberts, "Influence of Corneal Biomechanical Properties on Intraocular Pressure Measurement: Quantitative Analysis," J. Cataract. Refract. Surg. **31** (1), 146–155 (2005).
10. S. J. Kirkpatrick and M. J. Cipolla, "High Resolution Imaged Laser Speckle Strain Gauge for Vascular Applications," J. Biomed. Opt. **5** (1), 62–71 (2000).
11. D. Duncan and S. Kirkpatrick, "Performance Analysis of a Maximum-Likelihood Speckle Motion Estimator," Opt. Express. **10** (18), 927–941 (2002).
12. D. D. Duncan and S. J. Kirkpatrick," Processing Algorithms for Tracking Speckle Shifts in Optical Elastography of Biological Tissues," J. Biomed. Opt. **6** (4), 418–426 (2001).
13. S. Rigozzi, R. Müller, and J. G. Snedeker, "Local Strain Measurement Reveals a Varied Regional Dependence of Tensile Tendon Mechanics on Glycosaminoglycan Content," J. Biomechan. **42** (10), 1547–1552 (2009).
14. S. J. Kirkpatrick, R. K. Wang, D. D. Duncan, et al., "Imaging the Mechanical Stiffness of Skin Lesions by *in vivo* Acousto-Optical Elastography," Opt. Express. **14** (21), 9770–9779 (2006).
15. G. Le Goualher, A. Perchant, M. Genet, et al., *Towards Optical Biopsies with an Integrated Fibered Confocal Fluorescence Microscope* (Springer Berlin/Heidelberg, 2004).
16. J. G. Snedeker, A. Ben Arav, Y. Zilberman, et al., "Functional Fibered Confocal Microscopy: A Promising Tool for Assessing Tendon Regeneration," Tissue Eng., Part C **15** (3), 485–491 (2009).
17. J. Schmitt, "OCT Elastography: Imaging Microscopic Deformation Andstrain of Tissue," Opt. Express. **3** (6), 199–211 (1998).
18. J. Rogowska, N. Patel, S. Plummer, et al., "Quantitative Optical Coherence Tomographic Elastography: Method for Assessing Arterial Mechanical Properties," Br. J. Radiol. **79** (945), 707–711 (2006).
19. J. Rogowska, N. A. Patel, J. G. Fujimoto, et al., "Optical Coherence Tomographic Elastography Technique for Measuring Deformation and Strain of Atherosclerotic Tissues," Heart **90** (5), 556–562 (2004).
20. B. F. Kennedy, T. R. Hillman, R. A. McLaughlin, et al., "In vivo Dynamic Optical Coherence Elastography Using a Ring Actuator," Opt. Express. **17** (24), 21762–21772 (2009).
21. X. Liang, S. G. Adie, R. John, et al., "Dynamic Spectral-Domain Optical Coherence Elastography for Tissue Characterization," Opt. Express. **18** (13), 14183–14190 (2010).
22. X. Liang, A. L. Oldenburg, V. Crecea, et al., "Optical Micro-Scale Mapping of Dynamic Biomechanical Tissue Properties," Opt. Express. **16** (15), 11052–11065 (2008).
23. R. K. Wang, Z. Ma, and S. J. Kirkpatrick, "Tissue Doppler Optical Coherence Elastography for Real Time Strain Rate and Strain Mapping of Soft Tissue," Appl. Phys. Lett. **89** (14), 144103-3 (2006).
24. D. Alonso-Caneiro, K. Karnowski, B. J. Kaluzny, et al., "Assessment of Corneal Dynamics with High-Speed Swept Source Optical Coherence Tomography Combined with an Air Puff System," Opt. Express. **19** (15), 14188–14199 (2011).
25. C. Li, Z. Huang, and R. K. Wang, "Elastic Properties of Soft Tissue-Mimicking Phantoms Assessed by Combined Use of Laser Ultrasonics and Low Coherence Interferometry," Opt. Express. **19** (11), 10153–10163 (2011).
26. H.-J. Ko, W. Tan, R. Stack, et al., "Optical Coherence Elastography of Engineered and Developing Tissue," Tissue Eng. **12** (1), 63–73 (2006).
27. R. K. Manapuram, N. Sudheendran, V. R. Manne, et al., "3D Assessment of Mechanical Wave Propagation in the Crystalline Eye Lens Using PhS-SSOCT," Proc. SPIE **7885**, 78851V-9.
28. R. K. Manapuram, V. G. R. Manne, and K. V. Larin, "Phase-Sensitive Swept Source Optical Coherence Tomography for Imaging and Quantifying of Microbubbles in Clear and Scattering Media," J. Appl. Phys. **105** (10), 102040 (2009).
29. R. Manapuram, V. Manne, and K. Larin, "Development of Phase-Stabilized Swept-Source OCT for the Ultrasensitive Quantification of Microbubbles," Laser Phys. **18** (9), 1080–1086 (2008).
30. M. Gora, K. Karnowski, M. Szkulmowski, et al., "Ultra High-Speed Swept Source OCT Imaging of the Anterior Segment of Human Eye at 200 kHz with Adjustable Imaging Range," Opt. Express. **17** (17), 14880–14894 (2009).
31. T. J. Hall, M. Bilgen, M. F. Insana, et al., "Phantom Materials for Elastography, Ultrasonics, Ferroelectrics and Frequency Control," IEEE Trans. **44** (6), 1355–1365 (1997).